Improved Magnetic Resonance Image Reconstruction using Compressed Sensing and Adaptive Multi Extreme Particle Swarm Optimization Algorithm

Moureen Nalumansi[1], Elijah Mwangi[2] and George Kamucha[3]

[1]*Department of Electrical Engineering, Pan African University Institute for Basic Sciences, Technology and Innovation, Nairobi, Kenya; moureen.nalumansi@students.jkuat.ac.ke*
[2]*Faculty of Engineering, University of Nairobi, Kenya; elijah.mwangi@uonbi.ac.ke*
[3]*Faculty of Engineering, University of Nairobi, Kenya; gkamucha@uonbi.ac.ke*

*Correspondence: Moureen Nalumansi; moureen.nalumansi@students.jkuat.ac.ke

ABSTRACT- One powerful technique that can offer a thorough examination of the body's internal structure is magnetic resonance imaging (MRI). MRI's lengthy acquisition times, however, may restrict its clinical usefulness, particularly in situations where time is of the essence. Compressed sensing (CS) has emerged as a potentially useful method for cutting down on MRI acquisition times; nevertheless, the effectiveness of CS-MRI is dependent on the selection of the sparsity-promoting algorithm and sampling scheme. This research paper presents a novel method based on adaptive multi-extreme particle swarm optimization (AMEPSO) and dual tree complex wavelet transform (DTCWT) for fast image acquisition in magnetic resonance. The method uses AMEPSO in order to maximize the sampling pattern and minimize reconstruction error, while also exploiting the sparsity of MR images in the DTCWT domain to improve directional selectivity and shift invariance. MATLAB software was used for simulation of the proposed method. In comparison with the particle swarm optimized-DTCWT (PSODTCWT) and DTCWT algorithms, respectively, the results demonstrated an improvement in the peak signal-to-noise ratio of 8.92% and 15.92% and a higher structural similarity index measure of 3.69% and 7.5%. Based on these improvements, the proposed method could potentially make high-quality, real-time MRI imaging possible, which might improve detection and treatment of medical conditions and increase the throughput of MRI machines.

Keywords: Compressed sensing; Dual Tree Complex Wavelet Transform; Particle Swarm Optimization; Magnetic Resonance Imaging

1. INTRODUCTION

Magnetic resonance imaging (MRI), a non-ionizing radiation medical imaging technology [1] is widely utilized in medical procedures. However, the extensive data collection required for one image as necessitated by the Nyquist criterion [2], makes the process time-consuming, constrained by technical and physiological limitations [3] since more samples are needed for optimal resolution. To expedite data acquisition without compromising quality, data compression is a viable solution. Most natural signals, including those generated by human beings, exhibit sparsity in transform domains, enabling data representation with only a fewer number of significant coefficients [4]. Compressed sensing, resolving underdetermined systems, captures and reconstructs images from a small number of samples, making it suitable for MRI to significantly reduce acquisition times, benefiting patients with shorter scan durations [5][6]. Particularly valuable in high-resolution imaging like brain or musculoskeletal imaging, CS acquires a subset of k-space data [7], containing Fourier coefficients, to reconstruct images using sparsity-promoting algorithms. Since its discovery, CS has undergone extensive research, addressing challenges in sampling scheme design [8]. The choice of a sparsity-promoting algorithm is equally crucial and various schemes, such as random, pseudo-random, and deterministic methods, have been proposed in literature [9]. Algorithms like L_1-norm minimization and total variation minimization have been designed and their performance found to be dependent on image sparsity, structure, and noise levels [10].

In the realm of Compressed Sensing (CS) for Magnetic Resonance Imaging (MRI) reconstruction, various algorithms have been designed with the goal of efficiently reconstructing high-quality images from limited data, thereby reducing scanning time. A particle swarm optimized multilevel compression method was introduced in [11], with the MR image being divided into frames and computing the sparsity index after discrete cosine transform being performed. This

method showed ease in setting the different required peak signal-to-noise ratio (PSNR) values and compression levels (CL). However, there are difficulties in modelling the fitness function to maximize both the PSNR and CL values with this method.

A multi-rate approach for block-based CS using deep neural network was employed in [12]. This approach selectively assigns exclusive sampling rates for each block based on image information. Excellent abilities were shown relating to the reconstruction error correction and successful blocking artifact removal. However, because doing so would increase memory needs and computing complexity, the model cannot be directly extended to large-sized images, which raises questions regarding scalability and practical application.

In [13], an Efficient Wavelet Transform (EWT)-based MR image compression method with Grey Wolf Optimization (GWO) for parameter adjustment was presented. The images reconstructed with this approach have the maximum level of sharpness and edge preservation with highest artifacts removal being emphasized but the improvements are achieved at the expense of the central processing unit (CPU) time. Dual tree complex wavelet transform using wavelet tree sparsity was explored in [14]. The approach showed better enhancement when the two algorithms were examined separately but even at 20% sampling ratio, the achieved SNR of 18dB is still low and with insignificant visual enhancement.

The authors of [15] proposed a method called reconstruction partial Fourier (RecPF) which used the alternating direction method for signal reconstruction from partial Fourier measurements with complex-valued convolutional neural networks. Although it reduces the number of measurements, its speed is still not suitable for practical application with insignificant enhancement in the resolution compared to related works.

The Low-rank plus Sparse (L+S) with joint sparsity method enhancing free-breathing dynamic contrast-enhanced (DCE) MRI reconstruction was proposed in [16]. It modifies the traditional L+S approach by incorporating a temporal Fast Fourier Transform (FFT) constraint, boosting dynamic contrast performance. Fast Composite Splitting Algorithm (FCSA) efficiently solves the L+S model with multiple sparsity requirements. Testing on liver DCE-MRI datasets and simulations shows it outperforms Golden-angle Radial Sparse Parallel (GRASP) and standard L+S methods, increasing peak dynamic DCE signal by 24.8% and 33%, respectively. However, scaling to large datasets poses computational and memory challenges.

▨ 2. THEORETICAL FRAMEWORK

This section presents theories related to the proposed algorithm starting with a brief introduction on compressed sensing, magnetic resonance imaging and image quality evaluation.

2.1 Compressed sensing
Compressed sensing reduces data for faster acquisition, cost-effectiveness, and lower cost, given signal sparsity,

incoherence, and adherence to the restricted isometry property [17]. Sparsity refers to the property of a signal where a significant portion of its coefficients are zero or very close to zero when represented in a certain basis. This is crucial in CS because it allows for accurate reconstruction from a reduced set of measurements [18]. Let's consider a signal x that is sparse in a given basis Ψ, meaning that it can be represented by a sparse vector s, then the relationship can be expressed as $x = \Psi s$. The sparsity constraint is formulated as follows:

$$0 \leq \|s\|_0 \leq K \qquad (1)$$

where $\|s\|_0$ denotes the number of non-zero elements in the vector s, and K is a predefined sparsity level. The inequality expresses that the signal's sparse representation should have at most K non-zero coefficients [5]. However, the L_0-norm used in the above expression, counting the number of non-zero elements, is non-convex and computationally challenging to work with. Therefore, the L_1-norm is often used as a convex surrogate for sparsity, leading to a more tractable optimization problem [2].

$$\|s\|_1 = \sum_i |s_i| \qquad (2)$$

$$min\|s\|_1 \; subject \; to \; y = As \qquad (3)$$

where y represents the measurements obtained, A is the measurement matrix, and the objective is to find the sparsest solution (s) that still satisfies the measurement constraints.

Incoherence is a crucial concept in CS as it influences the success of the reconstruction process [19]. The goal is to have a measurement matrix that is incoherent with the sparsifying basis to facilitate accurate and robust signal recovery from a reduced set of measurements. The coherence between Ψ and A is quantified by the coherence parameter, often denoted as μ [20]. It is defined as the maximum absolute inner product between the columns of Ψ and the rows of A normalized by the square root of the signal length as shown in *Equation 4*. A low coherence, i.e., a small μ, implies that the sparsifying basis and the measurement matrix are relatively uncorrelated. This is desirable in compressed sensing because low coherence enhances the ability of matrix A to capture the sparse structure of the signal accurately. Mathematically, with ψ_i representing the ith column of the basis Ψ, and a_j representing the jth row of matrix A:

$$\mu = max_{i,j}|\langle\psi_i, a_j\rangle| \qquad (4)$$

The authors in [6] proposed a condition for the measurement matrix, A, known as the restricted isometry property (RIP). The RIP quantifies how well a matrix preserves the geometry of sparse vectors, ensuring that the measurements provide enough information for accurate signal reconstruction. The RIP having an order of K for A is expressed through the restricted isometry constant δ_k, where $0 < \delta_k < 1$. The RIP condition for order K asserts that the matrix A behaves almost like an isometry on all K-sparse vectors, meaning it approximately preserves their norm and pairwise distances enabling the recovery of the

original sparse signal from a reduced set of measurements [21]. Mathematically, for any K-sparse vector x, the RIP is characterized by the lower and upper bound conditions as shown in *Equation 5*. The lower bound condition, $(1 - \delta_k)\|x\|_2^2$, ensures that the squared norm of the sparse vector x is not significantly reduced by the action of A while the upper bound condition, $\|Ax\|_2^2 \leq (1 + \delta_k)\|x\|_2^2$, ensures that the squared norm of the measurement Ax is not significantly larger than that of the original sparse vector x. In a more compact form, the RIP condition for a matrix A of size mxn and order K can be expressed as follows:

$$(1 - \delta_k)\|x\|_2^2 \leq \|Ax\|_2^2 \leq (1 + \delta_k)\|x\|_2^2 \qquad (5)$$

Once the three conditions are satisfied (sparsity, incoherence and RIP), the signal can then be reconstructed using the inverse transform. In mathematical terms, the reconstructed signal, x_{rec}, is given by $x_{rec} = \Psi^{-1}s$ [22].

2.2 Magnetic Resonance Imaging

The fundamental principle of MRI is based on the behavior of atomic nuclei in the presence of strong magnetic fields and radiofrequency (RF) pulses. In an external magnetic field, certain atomic nuclei (e.g., hydrogen nuclei in the human body, abundant in water and fat) align with the magnetic field [1]. When exposed to RF pulses, these nuclei absorb energy and, upon relaxation, emit signals that can be detected to create detailed images.

During the RF pulse and signal acquisition, gradient magnetic fields G_x, G_y, G_z are applied to achieve spatial encoding. This results in different frequencies for different locations, providing spatial information whose equation is given by: $x(t) = \int G_x \, dt$ to illustrate how the position (x) is determined by integrating the gradient (G_x) over time [23]. However, during this process, the nuclei tend to spin towards the z-axis, to the equilibrium state, denoted as the M_0 or longitudinal magnetization. This leads to creation of poor-quality images hence the need to force the nuclei spins to deviate towards the transverse plane, leading to the generation of useful signals for imaging.

For excitation, RF pulses are applied to tip the aligned nuclear spins away from the z-axis and the tipping angle (θ) is determined by the flip angle of the RF pulse [24]. The Larmor equation describes the relationship between the angular frequency (ω) of precising nuclear magnetic moments and the magnetic field strength (B) as given in *Equation 6*.

$$\omega = \gamma B \qquad (6)$$

where ω is the Larmor frequency of precession, γ is the gyromagnetic ratio of the nucleus and B is the strength of the magnetic field. This equation establishes the relationship between the frequency of the RF pulse and the strength of the magnetic field, which is crucial for controlling the excitation of nuclear spins. Afterwards, the RF (receiver) coil detects signals emitted by relaxing nuclei during the relaxation processes, and this is a time-domain signal, usually represented by the free induction decay (FID) [25] signal which undergo Fourier Transform for image reconstruction. The FID is mathematically expressed in *Equations 7, 8 and 9* through the Bloch equations

in two main components of the longitudinal (M_z) and transverse magnetization (M_{xy}), which describe the behavior of nuclear magnetization in response to RF pulses and during relaxation processes.

$$\frac{dM_{xy}}{dt} = \gamma . B_{eff} . M_z - \frac{M_{xy}}{T_2} \qquad (7)$$

$$\frac{dM_z}{dt} = -\frac{M_z - M_0}{T_1} \qquad (8)$$

$$FID(t) = M_{xy}(t) = M_0 . e^{-t/T_2} . e^{i.\omega.t} \qquad (9)$$

where B_{eff} is the effective magnetic field, T_1 and T_2 are the longitudinal and transverse relaxation times, t is time, i is the imaginary unit and M_0 is the equilibrium magnetization.

2.3 Image Quality Measures

Using objective measures, the peak signal-to-noise ratio (PSNR) and the structure similarity index measure (SSIM) metrics were used to assess how well the suggested technique performs [26]. The PSNR is given by:

$$PSNR = 10 \log_{10}\left(\frac{L^2}{MSE}\right) \qquad (10)$$

$$\text{where,} \; MSE = \frac{\sum_{M,N}(x(m,n) - y(m,n))^2}{MN} \qquad (11)$$

where M and N are the total number of rows and columns in the input images, $x(m,n)$ and $y(m,n)$ are the original and reconstructed images respectively and L is the maximum variation in the input image data type.

To distinguish the similarity measuring task, the system uses three comparisons: luminance, contrast and structure to generate specific form of the SSIM for two images of local windows *x* and *y* given by:

$$SSIM(x,y) = \frac{(2\mu_x\mu_y + C_1)(2\sigma_{xy} + C_2)}{(\mu_x^2 + \mu_y^2 + C_1)(\sigma_x^2 + \sigma_y^2 + C_2)} \qquad (12)$$

where μ_x and μ_y are means of *x* and *y* respectively, σ_x^2 and σ_y^2 are variance values of *x* and *y* respectively, σ_{xy} is the covariance of *x*, *y* and C_1 and C_2 are constants introduced to eradicate the unstableness caused when SSIM denominator approaches zero.

3. THE PROPOSED COMPRESSED SENSING TECHNIQUE - AMEPSO ALGORITHM

In the proposed algorithm as illustrated in *Figure 1*, the Dual Tree Complex Wavelet Transform (DTCWT) is applied to the acquired k-space data, unveiling a sparse model in the wavelet domain. The Adaptive Multi Extreme Particle Swarm Optimization (AMEPSO) algorithm is used on the subsequent step to precisely navigate the complex search space inherent in sparse recovery problems. Through iterative updates, AMEPSO refines particle velocities and positions, optimizing the fitness function depending on the L_1 norm. The algorithm converges to unveil the optimal solution, representing the reconstructed

image. Finally, the inverse DTCWT is applied, transforming the solution back into the spatial domain, yielding a reconstructed image of remarkable fidelity. This integrated approach reveals the benefits of a combined CS, DTCWT, and AMEPSO approach in advancing the frontier of rapid and accurate medical image reconstruction.
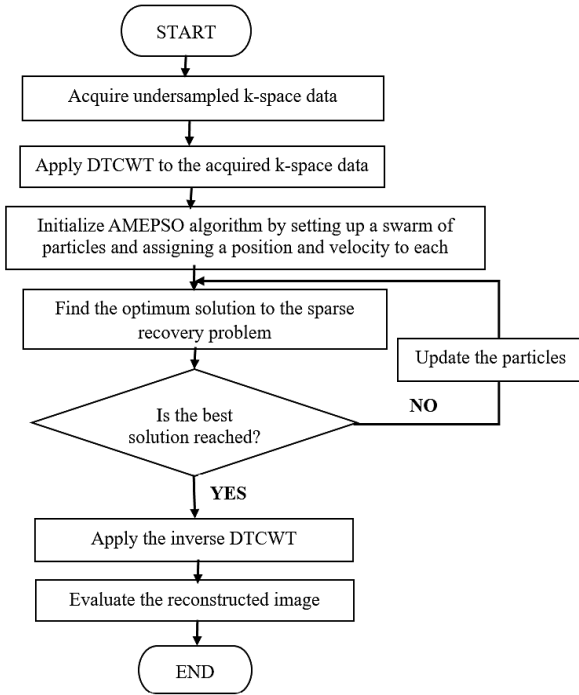

Figure 1. Flow chart of the proposed algorithm

3.1. Compressed Sensing based Dual Tree Complex Wavelet Transform

The Complex Wavelet Transform (CWT) employs analytic filters to decompose signals in the transform domain into real and imaginary components, facilitating precise energy localization of oscillating functions [27]. The wavelet basis computes amplitude, phase, and real and imaginary coefficients, enhancing the discrete wavelet transform (DWT). The Dual Tree Complex Wavelet Transform (DTCWT) improves on DWT by employing two parallel decimated trees with real-valued coefficients, enabling perfect image reconstruction [28]. DTCWT captures features at various scales and orientations using two wavelet filters in a dyadic tree structure [29]. This dual-tree arrangement is shown in *Figure 2*, with one set shifted by a half sample, yields complex-valued signals, allowing representation of both phase and magnitude information in the signal [30]. Iterative decomposition produces a multiresolution of an input signal denoted by *x(n)* which is under sampled with a two factor at each stage. In the upper tree, there is the low-pass and high-pass filters representing the real part denoted by $h_0(n)$ and $h_1(n)$ respectively. Similarly, the lower tree includes corresponding filters, $g_0(n)$ and $g_1(n)$ representing the low-pass and high-pass filters, which pertain to the imaginary part. The DTCWT exhibits enhanced directional selectivity, reduced redundancy, and improved shift invariance.
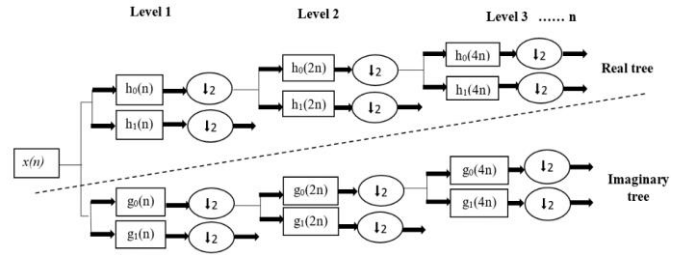

Figure 2. Forward transformation of the Dual Tree Complex Wavelet Transform

During Compressed Sensing, the DTCWT involves steps as illustrated in *Figure 3*. The wavelet coefficient matrix, **W**, undergoes thresholding for signal sparsity with the operation given in *Equations 13, 14 and 15* as [31]:

$$Soft\ threshold = \frac{sign(W) \cdot max(|W| - T, 0)}{|W|} \quad (13)$$

$$Threshold, T = \sigma^2 \sqrt{\left(\frac{2\log_{10}(k)}{L}\right)} \quad (14)$$

$$\sigma = \text{Median}(|W|)/0.6745 \quad (15)$$

where the expression *max(|W|−T,0)* calculates the maximum of the absolute value of each element in *W* from *T* and 0 setting all negative values resulting from subtraction to zero, *k* and *L* are the coefficients and maximum pixels in the signal respectively, sigma, *σ*, is the noise level estimated using the Median Absolute Deviation (MAD) [32].

0.6745 is the 0.75th quantile of the normal distribution used as a scaling factor that aligns the MAD with the standard deviation. It ensures consistency of MAD as a standard deviation estimator, facilitating robustness against outliers and maintaining sensitivity to extreme values.
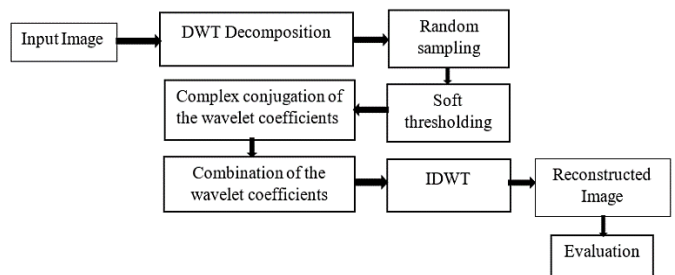

Figure 3. Block diagram of the DTCWT Algorithm

3.2 Adaptive Multi Extreme Particle Swarm Optimization

Particle Swarm Optimization (PSO) mimics the movement of a school of fish or birds in a space that is multidimensional to find optimal solutions. PSO involves particles with fitness, velocities, and positions values in a swarm exploring the search field where the movements are guided by attraction towards personal and global best positions, aiming for the best solution. However, standard PSO struggles with multiple extrema in the

global range, impacting sparse signal reconstruction in compressed sensing [33].

Addressing this, an Adaptive Multi-Extreme Particle Swarm Optimization (AMEPSO) is proposed which uses a multi-extreme approach to enhance solution search. Adaptive parameters regulate the local search probability to fit the profitability of each individual particle, ensuring a fair trade-off between extraction and exploration [34]. By quickly identifying strong scattering zones, AMEPSO speeds up the objective function solution and enhances imaging quality during sparse target image scanning.

By managing the balance between exploring and profiting in the algorithm, the constriction coefficient approach employed for selecting PSO parameters, helps keep the particles from moving too quickly and improves convergence and stability. This ultimately helps to create a sparse representation, which lowers artifacts in reconstructed images. *Figure 4* illustrates the flow of the AMEPSO algorithm.
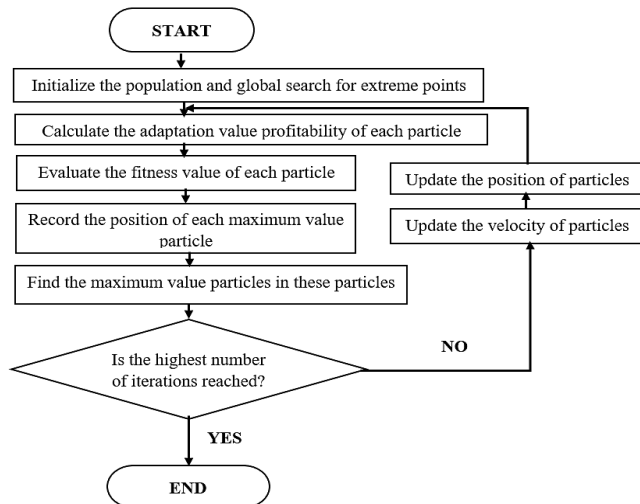

Figure 4. Flow-chart of the AMEPSO Algorithm

The particle positions and velocities are updated iteratively as indicated in *Equations 16 and 17* respectively [35].

$$v(i)_{n+1} = wv(i)_n + C_1 R_1 (pbest(i)_n - x(i)_n) + C_2 R_2 (gbest_n - x(i)_n) \quad (16)$$

$$x(i)_{n+1} = x(i)_n + v(i)_{n+1}\delta(t) \quad (17)$$

where w is the inertia weight, C_1 and C_2 are the acceleration constants, R_1 and R_2 are random positive numbers less than one, $pbest(i)_n$ and $gbest_n$ are the best position of particle i and the whole swarm respectively up to the nth iteration and $\delta(t)$ is the time step.

Higher-probability particles, likely in strong scattering regions, enhance local search in these areas. Adaptive parameters, including inertia weight (w) and acceleration constants (C_1 and C_2), are updated to balance exploration and exploitation. *Equations 18, 19 and 20* specify the dynamic parameter adjustments throughout iterations, ensuring effective

optimization in AMEPSO. The parameter rates are controlled by constants, providing a flexible and adaptive optimization process over the iterations.

$$w_{n+1} = w_{min} + (w_{max} - w_{min})\left(1 - \frac{n}{N}\right)^p \quad (18)$$

$$C_{1\,(n+1)} = C_{1\,min} + (C_{1\,max} - C_{1\,min})\frac{n}{N} \quad (19)$$

$$C_{2\,(n+1)} = C_{2\,max} - (C_{2\,max} - C_{2\,min})\frac{n}{N} \quad (20)$$

where w_{min}, $C_{1\,min}$, $C_{2\,min}$ are the minimum values of the inertia weight, acceleration constants C_1 and C_2 respectively while, w_{max}, $C_{1\,max}$, $C_{2\,max}$ are the maximum values, N is the maximum number of iterations, n is the current iteration, and p is a constant that controls the rate of change of the inertia weight. A higher p might lead to stronger exploitation and less exploration whereas a lower p might result in more exploration and less exploitation allowing the algorithm to explore a larger portion of the search field.

4. RESULTS AND DISCUSSIONS

Simulations were carried out using MATLAB R2023a on a PC with 16GB RAM and core i7 processor and the results were used to examine and illustrate the performance of the proposed technique. This study included six MR images (head, ankle, knee, spine, shoulder, and brain) got from MR databases [36][37]. 40 iterations, an under-sampling factor of 0.7, and a convergence threshold of 1e-5 were used for the evaluation. Additionally, two decomposition levels and coif5 wavelet type were used in this work.

The reference images are displayed in column (a) of *Figure 5*. These are subsequently employed in DWT, DTCWT, PSODTCWT, and the suggested method in columns (b), (c), (d), and (e), in that order. Using DWT, DTCWT, PSODTCWT, and the proposed method for reconstruction of the ankle, the images have PSNRs of 21.62dB, 21.91dB, 22.89dB, and 25.47dB, respectively.
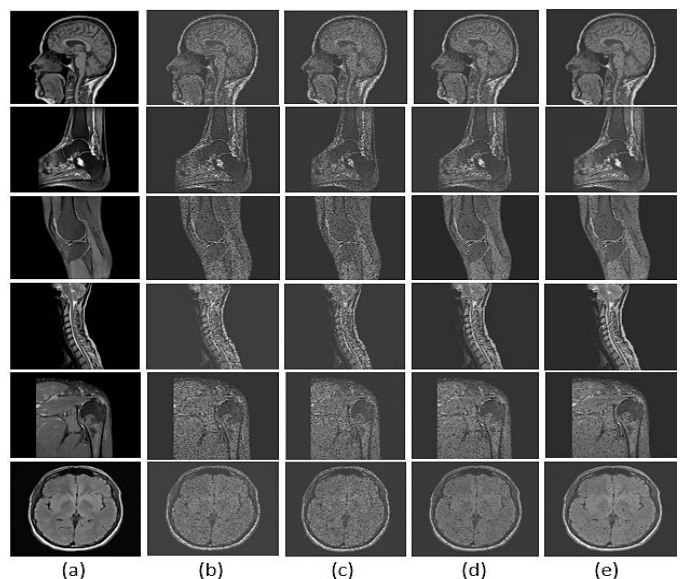

| (a) | (b) | (c) | (d) | (e) |

Figure 5. Image reconstruction using different selected compressed sensing (a) Ground-truth image (b) DWT (c) DTCWT (d) PSODTCWT (e) Proposed method
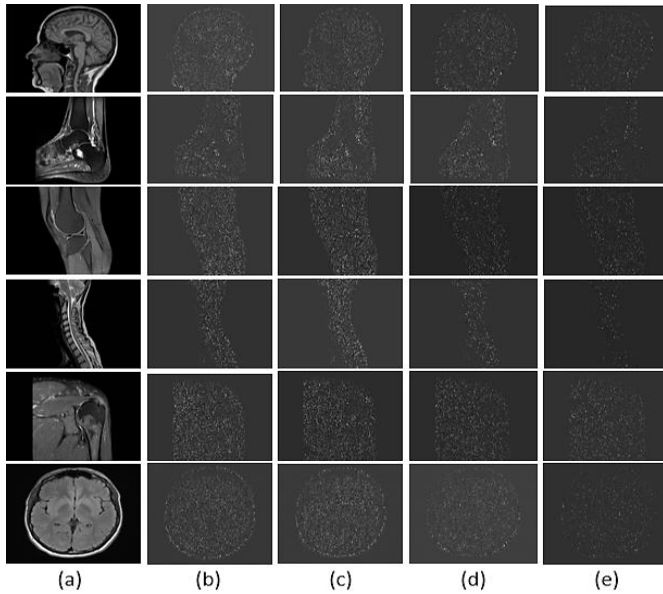
Figure 6. Difference images resulting from the comparisons of the reference and reconstructed images using different selected compressed sensing methods (a) Ground-truth image (b) DWT (c) DTCWT (d) PSODTCWT (e) Proposed method

As observed, there is insignificant visual difference between images reconstructed using the classical DWT, DTCWT and PSODTCWT with both images being affected with artifacts which could reduce their credibility. However, with similar parameters, the proposed method reconstructed the images as close to the ground truth images as possible with residues in the difference images which can be ignored as illustrated in Figure 6.

Table 1 displays the results for the head, ankle, knee, spine, shoulder and brain MR images using the proposed, DWT, DTCWT and PSODTCWT methods at different under-sampling factors. PSNR with SSIM quality assessment indices are used and it can be observed that the images reconstructed with the proposed algorithm have higher PSNR and SSIM values than DWT, DTCWT and PSODTCWT methods for all the under-sampling factors.

For example, at 0.6 under-sampling factor, the proposed method has approximately 1.62dB, 1.49dB and 0.75dB PSNR with 0.03, 0.02 and 0.02 SSIM improvements over PSODTCWT for the knee, spine and brain MR images respectively. These improvements indicate a high degree of similarity and fidelity between compared images, suggesting good quality and effective preservation of structural information.

Table 1. Performance evaluation using PSNR and SSIM metrics on the proposed method at different under-sampling factors

MR Images	Under-sampling Factor	DWT PSNR (dB)	DWT SSIM	DTCWT PSNR (dB)	DTCWT SSIM	PSODTCWT PSNR (dB)	PSODTCWT SSIM	Proposed PSNR (dB)	Proposed SSIM
	0.6	18.86	0.84	19.30	0.85	20.63	0.89	21.36	0.91
	0.7	19.29	0.85	19.78	0.87	21.56	0.91	23.43	0.93
	0.8	19.73	0.87	20.22	0.88	22.19	0.92	23.59	0.94
	0.9	20.23	0.88	20.74	0.90	22.27	0.92	25.37	0.96
	0.6	20.74	0.86	21.19	0.87	22.72	0.91	24.07	0.94
	0.7	21.20	0.87	21.68	0.89	22.79	0.91	25.05	0.95
	0.8	21.69	0.89	22.21	0.90	23.39	0.93	25.53	0.95
	0.9	22.15	0.90	22.74	0.91	24.12	0.93	27.29	0.97
	0.6	21.02	0.86	21.47	0.87	22.11	0.89	23.73	0.92
	0.7	21.48	0.87	21.80	0.88	24.18	0.93	24.62	0.94
	0.8	21.82	0.88	22.44	0.90	24.78	0.93	25.45	0.95
	0.9	22.39	0.90	22.94	0.91	25.28	0.94	26.77	0.96
	0.6	21.10	0.89	21.45	0.90	22.62	0.92	24.11	0.94
	0.7	21.56	0.90	22.01	0.91	23.74	0.94	24.90	0.95
	0.8	22.15	0.91	22.45	0.92	24.32	0.94	28.37	0.98
	0.9	22.83	0.92	23.24	0.93	28.18	0.97	30.84	0.99
	0.6	19.65	0.84	20.03	0.85	21.26	0.89	21.57	0.90
	0.7	20.03	0.85	20.46	0.87	21.89	0.90	23.72	0.93
	0.8	20.54	0.87	21.00	0.88	22.77	0.92	24.31	0.94
	0.9	21.05	0.88	21.60	0.90	23.08	0.94	27.07	0.97
	0.6	16.87	0.80	17.30	0.82	18.54	0.86	19.29	0.88
	0.7	17.30	0.82	17.75	0.84	18.71	0.86	20.73	0.91
	0.8	17.75	0.84	18.30	0.86	18.99	0.87	22.89	0.94
	0.9	18.23	0.85	18.83	0.87	21.26	0.91	23.33	0.94

Figure 7 represents the performance of DWT, DTCWT, PSODTCWT and the proposed method using the PSNR metric. The proposed method outperforms PSODTCWT and DTCWT with PSNR values averaging to 8.92% and 15.92% improvements respectively. These improvements correspond to 8.92% an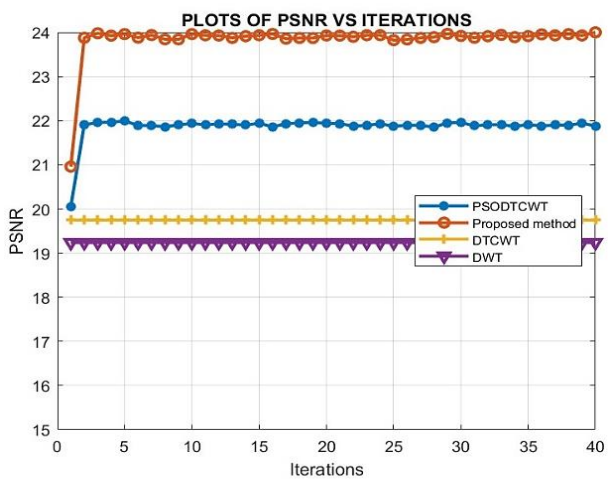d 15.92% reduction in the scan duration when compared with PSODTCWT and DTCWT. The performance evaluation is also carried out using SSIM metric as provided in *Figure 8*. While all the methods exhibit good values above 0.8 SSIM, the proposed method outperforms PSODTCWT and DTCWT by 3.69% and 7.5%, respectively.
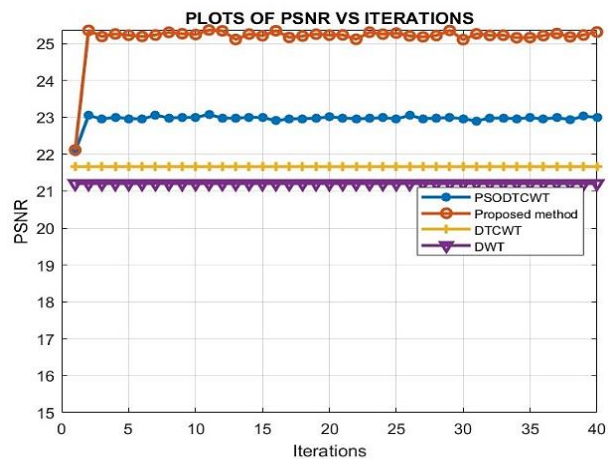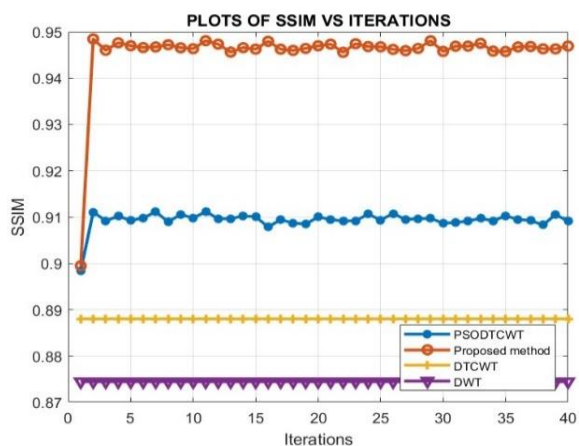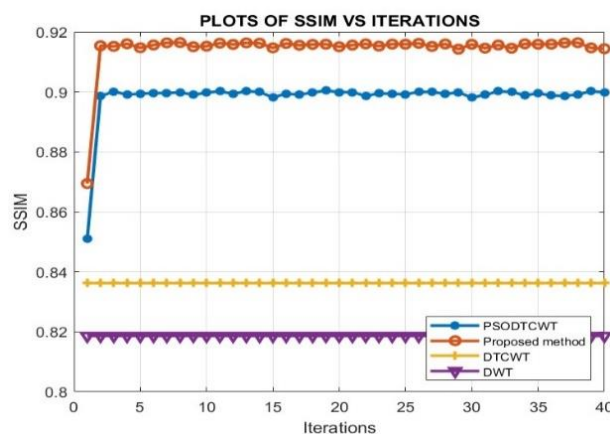
(a)
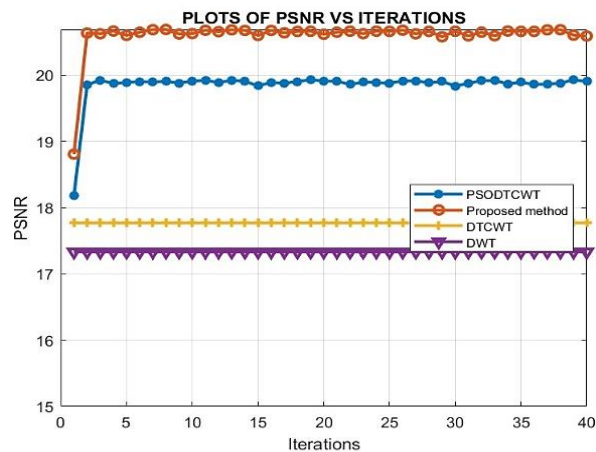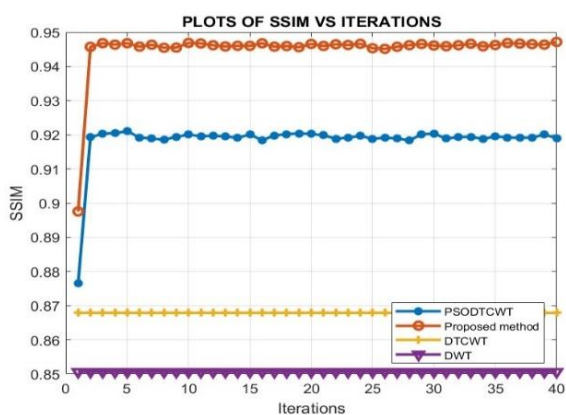
(b)

(c)
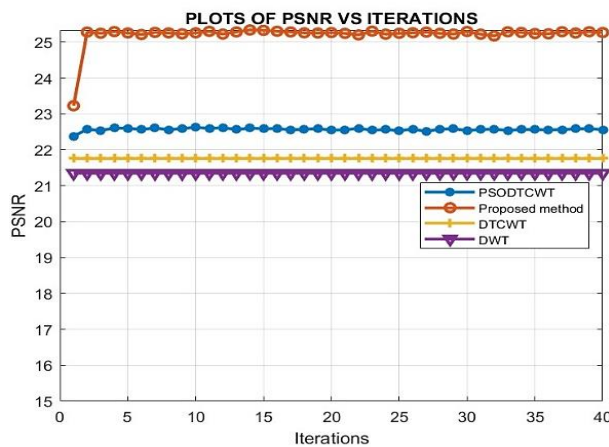
(d)
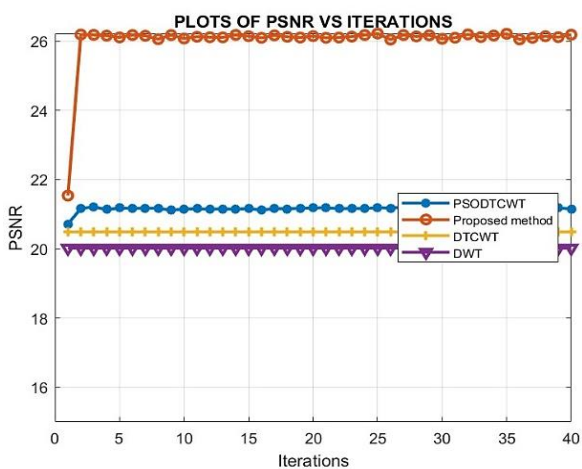
(e)
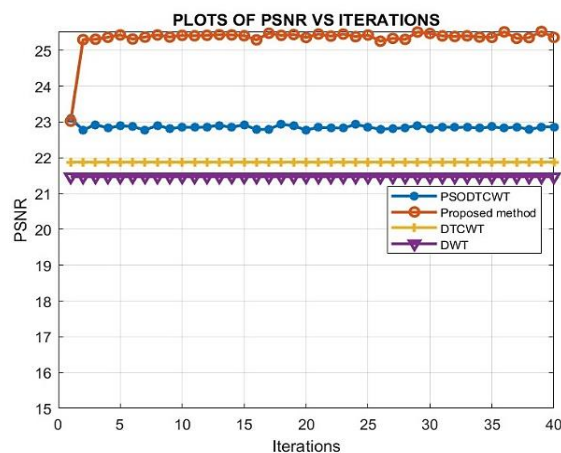
(f)

Figure 7. PSNR evaluation of different selected methods with the proposed method on the MR images (a) head (b) brain (c) knee (d) spine (e) shoulder (f) ankle
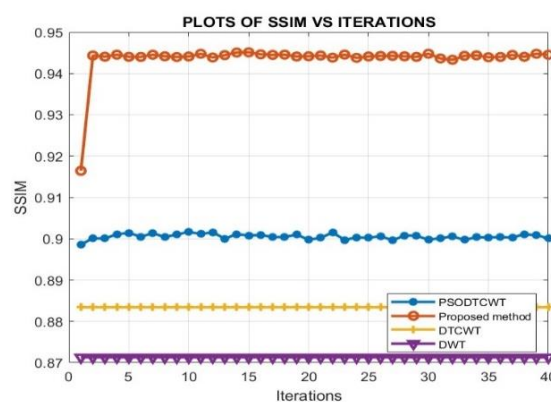
(a)

(b)

(c)

(d)

(e)

(f)

Figure 8. SSIM evaluation of different selected methods with the proposed method on the MR images (a) head (b) brain (c) knee (d) spine (e) shoulder (f) ankle
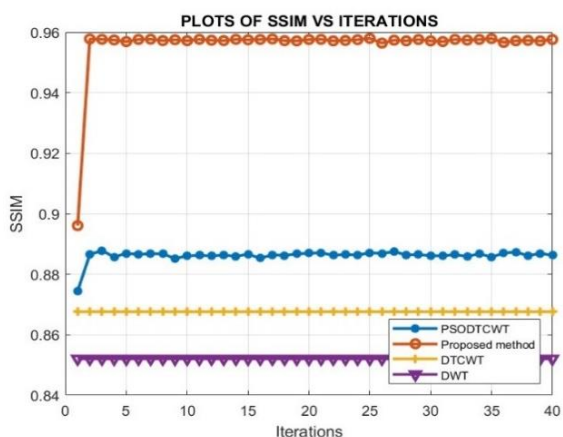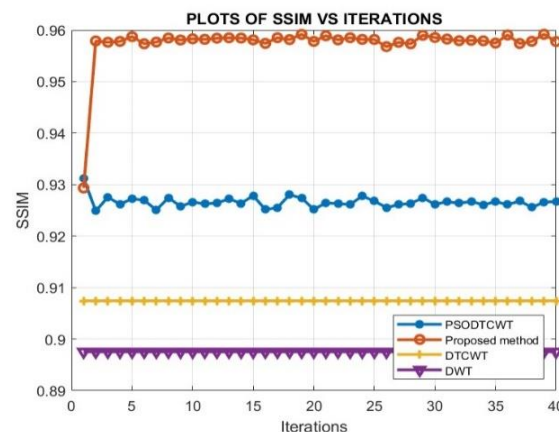
5. CONCLUSION

An adaptive multi extreme particle swarm optimized compressed sensing technique in MRI reconstruction has been presented in this paper. MATLAB simulations have been used with the results showing improvements in the image quality of 8.92% and 3.69% for PSNR and SSIM respectively, over the PSODTCWT method. These improvements correspond to approximately 8.92% reduction in the scan duration. Despite

the efficiency improvements achieved, future research work will involve experiments with different filter functions to further remove artifacts in the reconstructed images.

Acknowledgments

REFERENCES

[1] P. Wangaryattawanich, A. M. Rutman, S. Petcharunpaisan, and M. Mossa-Basha, "Incidental findings on brain magnetic resonance imaging (MRI) in adults: a review of imaging spectrum, clinical significance, and management," *The British Journal of Radiology*, vol. 96, no. 1142, Feb. 2023, doi: 10.1259/bjr.20220108.

[2] M. A. G. Duff, I. J. A. Simpson, M. J. Ehrhardt, and N. D. F. Campbell, "VAEs with structured image covariance applied to compressed sensing MRI," *Physics in Medicine and Biology*, vol. 68, no. 16, 2023, doi: 10.1088/1361-6560/ace49a.

[3] V. M. Runge, J. K. Richter, and J. T. Heverhagen, "Speed in Clinical Magnetic Resonance," *Investigative Radiology*, vol. 52, no. 1, pp. 1–17, 2017, doi: 10.1097/RLI.0000000000000330.

[4] D. S. Taubman and M. W. Marcellin, "JPEG2000: Standard for interactive imaging," *Proceedings of the IEEE*, vol. 90, no. 8, pp. 1336–1357, Aug. 2002, doi: 10.1109/JPROC.2002.800725.

[5] D. L. Donoho, "Compressed sensing," *IEEE Transactions on Information Theory*, vol. 52, no. 4, pp. 1289–1306, Apr. 2006, doi: 10.1109/TIT.2006.871582.

[6] E. J. Candes, J. Romberg, and T. Tao, "Robust uncertainty principles: exact signal reconstruction from highly incomplete frequency information," *IEEE Transactions on Information Theory*, vol. 52, no. 2, pp. 489–509, Feb. 2006, doi: 10.1109/TIT.2005.862083.

[7] G. Yiasemis, C. I. Sánchez, J.-J. Sonke, and J. Teuwen, "On retrospective k-space subsampling schemes for deep MRI reconstruction," *Magnetic Resonance Imaging*, vol. 107, no. 1, pp. 33–46, Apr. 2024, doi: 10.1016/j.mri.2023.12.012.

[8] D. Singh, A. Monga, H. L. de Moura, X. Zhang, M. V. W. Zibetti, and R. R. Regatte, "Emerging Trends in Fast MRI Using Deep-Learning Reconstruction on Undersampled k-Space Data: A Systematic Review," *Bioengineering*, vol. 10, no. 9, p. 1012, Aug. 2023, doi: 10.3390/bioengineering10091012.

[9] M. Gammoudi, C. Scheunert, G. T. Nguyen, and F. Fitzek, "Practical construction of sensing matrices for a greedy sparse recovery algorithm over finite fields," in *2023 Data Compression Conference (DCC)*, Snowbird, Utah, USA: IEEE, Mar. 2023, pp. 120–129. doi: 10.1109/DCC55655.2023.00020.

[10] L. Feng, T. Benkert, K. T. Block, D. K. Sodickson, R. Otazo, and H. Chandarana, "Compressed sensing for body MRI," *Journal of Magnetic Resonance Imaging*, vol. 45, no. 4, pp. 966–987, Apr. 2017, doi: 10.1002/jmri.25547.

[11] T. Tashan and A. K. Kadhim, "Particle swarm optimization based multilevel MRI compression using compressive sensing," *Bulletin of Electrical Engineering and Informatics*, vol. 11, no. 5, pp. 2621–2628, 2022, doi: 10.11591/eei.v11i5.3873.

[12] E. U. Haq, H. Jianjun, X. Huarong, and K. Li, "Block-based compressed sensing of MR images using multi-rate deep learning approach," *Complex and Intelligent Systems*, vol. 7, no. 5, pp. 2437–2451, 2021, doi: 10.1007/s40747-021-00426-6.

[13] M. Ragab, O. A. Omer, and M. Abdel-Nasser, "Compressive sensing MRI reconstruction using empirical wavelet transform and grey wolf optimizer," *Neural Computing and Applications*, vol. 32, no. 7, pp. 2705–2724, 2020, doi: 10.1007/s00521-018-3812-7.

[14] M. Ragab, O. A. Omer, and H. S. Hussien, "Compressive sensing MRI using dual tree complex wavelet transform with wavelet tree sparsity," in *2017 34th National Radio Science Conference (NRSC)*, Alexandria, Egypt: IEEE, Mar. 2017, pp. 481–486. doi: 10.1109/NRSC.2017.7893519.

[15] L. Xiao, Y. Liu, Z. Yi, Y. Zhao, L. Xie, and P. Cao, "Partial Fourier reconstruction of complex MR images using complex-valued convolutional neural networks," *Magnetic Resonance in Medicine*, vol. 87, no. 2, pp. 999–1014, Feb. 2022, doi: 10.1002/mrm.29033.

[16] J. Zhang, F. Najeeb, X. Wang, P. Xu, H. Omer, and J. Zheng, "Improved Dynamic Contrast-Enhanced MRI Using Low Rank With Joint Sparsity," *IEEE Access*, vol. 10, no. November 2022, pp. 121193–121203, 2022, doi: 10.1109/ACCESS.2022.3222313.

[17] S. Guruprasad, S. H. Bharathi, and D. Anto Ramesh Delvi, "Effective compressed sensing MRI reconstruction via hybrid GSGWO algorithm," *Journal of Visual Communication and Image Representation*, vol. 80, p. 103274, Oct. 2021, doi: 10.1016/j.jvcir.2021.103274.

[18] Y. Xie and Q. Li, "A Review of Deep Learning Methods for Compressed Sensing Image Reconstruction and Its Medical Applications," *Electronics*, vol. 11, no. 4, p. 586, Feb. 2022, doi: 10.3390/electronics11040586.

[19] J. Lang, C. Zhang, and D. Zhu, "Undersampled MRI reconstruction based on spectral graph wavelet transform," *Computers in Biology and Medicine*, vol. 157, no. 2, p. 106780, May 2023, doi: 10.1016/j.compbiomed.2023.106780.

[20] T. Hermans, K. Carkeek, A. Dereymaeker, K. Jansen, G. Naulaers, and S. Van Huffel, "Partial wavelet coherence as a robust method for assessment of neurovascular coupling in neonates with hypoxic ischemic encephalopathy," *Scientific Reports*, vol. 13, no. 1, p. 457, Jan. 2023, doi: 10.1038/s41598-022-27275-8.

[21] Q. Chen, N. J. Shah, and W. A. Worthoff, "Compressed Sensing in Sodium Magnetic Resonance Imaging: Techniques, Applications, and Future Prospects," *Journal of Magnetic Resonance Imaging*, vol. 55, no. 5, pp. 1340–1356, May 2022, doi: 10.1002/jmri.28029.

[22] J. Huang, L. Wang, and Y. Zhu, "Compressed Sensing MRI Reconstruction with Multiple Sparsity Constraints on Radial Sampling," *Mathematical Problems in Engineering*, vol. 2019, 2019, doi: 10.1155/2019/3694604.

[23] D. Qiu, Y. Cheng, and X. Wang, "Progressive Feedback Residual Attention Network for Cardiac Magnetic Resonance Imaging Super-Resolution," *IEEE Journal of Biomedical and Health Informatics*, vol. 27, no. 7, pp. 3478–3488, Jul. 2023, doi: 10.1109/JBHI.2023.3272155.

[24] S. Geethanath and J. T. Vaughan, "Accessible magnetic resonance imaging: A review," *Journal of Magnetic Resonance Imaging*, vol. 49, no. 7, pp. e65–e77, 2019, doi: 10.1002/jmri.26638.

[25] C. Baishya, R. N. Premakumari, M. E. Samei, and M. K. Naik, "Chaos control of fractional order nonlinear Bloch equation by utilizing sliding mode controller," *Chaos, Solitons & Fractals*, vol. 174, no. 3, p. 113773, Sep. 2023, doi: 10.1016/j.chaos.2023.113773.

[26] B. Vasudeva, P. Deora, S. Bhattacharya, and P. M. Pradhan, "Compressed Sensing MRI Reconstruction with Co-VeGAN: Complex-Valued Generative Adversarial Network," in *2022 IEEE/CVF Winter Conference on Applications of Computer Vision (WACV)*, Waikoloa, HI, USA: IEEE, Jan. 2022, pp. 1779–1788. doi: 10.1109/WACV51458.2022.00184.

[27] B. P. P. Kumar, P. K. B. Rangaiah, and R. Augustine, "Enhancing Medical Image Reclamation for Chest Samples Using B-Coefficients, DT-CWT and EPS Algorithm," *IEEE Access*, vol. 11, pp. 113360–113375, 2023, doi: 10.1109/ACCESS.2023.3322205.

[28] E. Hancer and A. Subasi, "EEG-based emotion recognition using dual tree complex wavelet transform and random subspace ensemble classifier," *Computer Methods in Biomechanics and Biomedical Engineering*, vol. 26, no. 14, pp. 1772–1784, Oct. 2023, doi: 10.1080/10255842.2022.2143714.

[29] D. Wu, L. Li, J. Wang, P. Ma, Z. Wang, and H. Wu, "Robust zero-watermarking scheme using DT CWT and improved differential entropy for color medical images," *Journal of King Saud University - Computer and Information Sciences*, vol. 35, no. 8, p. 101708, Sep. 2023, doi: 10.1016/j.jksuci.2023.101708.

[30] D. Bhonsle, A. G. Pillai, T. Rizvi, R. Mishra, A. K. Sahu, and R. Mishra, "White Gaussian Noise Removal From Computed Tomography Images Using Python," in *2024 Fourth International Conference on Advances in Electrical, Computing, Communication and Sustainable Technologies (ICAECT)*, Bhilai, India: IEEE, Jan. 2024, pp. 1–5. doi: 10.1109/ICAECT60202.2024.10468832.

[31] B. Qu, Z. Zhang, Y. Chen, C. Qian, and T. Kang, "A convergence analysis for projected fast iterative soft-thresholding algorithm under radial sampling MRI," *Journal of Magnetic Resonance*, vol. 351, p. 107425, Jun. 2023, doi: 10.1016/j.jmr.2023.107425.

[32] Y. Li, Z. Li, K. Wei, W. Xiong, J. Yu, and B. Qi, "Noise estimation for image sensor based on local entropy and median absolute deviation," *Sensors (Switzerland)*, vol. 19, no. 2, 2019, doi: 10.3390/s19020339.

[33] L. Zhu, M. Liu, and W. H. Shao, "MMW compressed sensing target reconstruction based on AMPSO search algorithm," *Journal of Electromagnetic Waves and Applications*, vol. 34, no. 16, pp. 2094–2106, 2020, doi: 10.1080/09205071.2020.1809018.

[34] Y. Song, Y. Liu, H. Chen, and W. Deng, "A Multi-Strategy Adaptive Particle Swarm Optimization Algorithm for Solving Optimization Problem," *Electronics (Switzerland)*, vol. 12, no. 3, 2023, doi: 10.3390/electronics12030491.

[35] C. Qin, Y. Zhang, F. Bao, C. Zhang, P. Liu, and P. Liu, "XGBoost optimized by adaptive particle swarm optimization for credit scoring," *Mathematical Problems in Engineering*, vol. 2021, 2021, doi: 10.1155/2021/6655510.

[36] T. Foster and B. Di Muzio, "Normal MRI Brain," in *Radiopaedia.org*,

Radiopaedia.org, 2015. doi: 10.53347/rID-39311.

[37] Siemens Healthineers, "Magnetic resonance imaging-Magnetom World." Accessed: May 23, 2023. [Online]. Available: https://www.magnetomworld.siemens-healthineers.com/clinical-corner/protocols/dicom-images